

This is the final draft of the contribution published as:

Magri, F., Möller, S., Inbar, N., Möller, P., Raggad, M., Rödiger, T., Rosenthal, E., Siebert, C. (2016):

2D and 3D coexisting modes of thermal convection in fractured hydrothermal systems - implications for transboundary flow in the Lower Yarmouk Gorge

Mar. Pet. Geol. **78** , 750 - 758

The publisher's version is available at:

<http://dx.doi.org/10.1016/j.marpetgeo.2016.10.002>

1 **2D and 3D coexisting modes of thermal convection in fractured hydrothermal systems - implications**
2 **for transboundary flow in the Lower Yarmouk Gorge**

3
4 F. Magri^{1,2}, S. Möller², N. Inbar³, P. Möller⁴, M. Raggad⁵, T. Rödiger⁶, E. Rosenthal³, and C. Siebert⁶

5 1 Helmholtz Centre for Environmental Research - UFZ Dept. of Environmental Informatics (ENVINF), Permoserstraße 15, 04318
6 Leipzig, Germany; fabien.magri@ufz.de

7 2 Freie Universität Berlin, Hydrogeology, Berlin, Germany

8 3 Tel Aviv University, The Department of Geophysics and Planetary Sciences, Tel Aviv, Israel

9 4 GFZ German Research Centre for Geosciences, Potsdam, Germany

10 5 University of Jordan, Faculty of Science, Amman, Jordan

11 6 Helmholtz Centre for Environmental Research – UFZ, Dept. Catchment Hydrology, Halle, Germany

12

13 **Abstract**

14 Numerical investigations of 2D and 3D modes of large-scale convection in faulted aquifers are presented
15 with the aim to infer possible transport mechanisms supporting the formation of thermal springs
16 through fractured aquicludes. The transient finite elements models are based on idealized structural
17 features that can characterize many hydrothermal systems. The sensitivity analysis of the fault
18 permeability showed that faults cross-cutting the main regional flow direction allow groundwater to be
19 driven laterally by convective forces within the fault planes. Therein thermal waters can either discharge
20 along the fault traces or exit the fault through adjacent permeable aquifers. In the latter case, the
21 resulting flow is helicoidally and transient. The location and the spacing between discharge areas can
22 migrate with time, is not strictly constrained to the damage zones and reflects the wavelength of the
23 multicellular regime in the fault zone.

24 An illustrative example based on a simplified structural data of the Lower Yarmouk Gorge (LYG) is
25 presented. The numerical calculations indicate that crossing flow paths result from the coexistence of
26 fault convection, developing for example along NE-SW oriented faults within the Gorge, and additional
27 flow fields. The latter are induced either by topography N-S gradients, e.g. perpendicular to the major
28 axe of the Gorge, or by local thermal convection in permeable aquifers below the Eocene aquiclude.

29 Sensitivity analysis of fault hydraulic conductivity (K) and the analytical solutions based on viscous-
30 dependent Rayleigh theory show that K values between $2.3e^{-7}$ m/s and $9.3e^{-7}$ m/s (i.e. 7 m/yr and
31 30 m/yr, respectively) favor coexisting transport processes. The uprising thermal plumes spread over
32 several hundred meters forming clusters of springs, in agreement with observation, and which
33 temperature fall within the measured ranges, i.e. 20°C – 60°C . To some extent the models also
34 reproduced the transient behavior of the spring temperature. Owing to the idealized nature of the
35 presented models, the numerical results and the associated analytical solution can be applied to study
36 the onset of thermal convection and resulting flow patterns of any fractured hydrothermal basin.

37 **1. Introduction**

38 In most hydrothermal systems, the dependence of fluid density on temperature leads to unstable
39 density stratifications in which a colder (denser) fluid overlies a warmer (lighter) fluid (Nield and Bejan,
40 2006). The resulting convective flow is also referred to as buoyancy-driven flow or thermally-induced
41 flow. Since density differences can extend over large spatial scales and persist over geological time
42 periods, thermal convection is often invoked to explain natural processes in sedimentary basins such as
43 dolomitization (Gasparrini et al., 2006), hydrothermal mineralization (Kühn M. & Gessner K. 2009;
44 Harcouët-Menou et al., 2009), seawater intrusion (Magri et al., 2012) or CO_2 dissolution (Bickle, 2009).
45 Early studies of the problem highlight that the onset of thermal convection in the Earth crust requires a
46 relatively high permeability of the rocks (Lapwood, 1948). Accordingly, thermally-induced flow develops
47 in permeable faults or fractures. Analytical calculations from Malkovsky and Pek (2004) show that, under
48 a normal geothermal gradient ($0.025^{\circ}\text{C}/\text{m}$), a damage zone of 100 m width embedded in an impervious
49 rock allows for convection already at hydraulic conductivity of $1 e^{-7}$ m/s. Several numerical models
50 suggest that thermal convection in faulted basins can explain the spatial correlation between fractured
51 zones and heat flow anomalies or the occurrence of hot springs (e.g., Ormond et al., 1995; Rabinowicz et
52 al., 1999; Person et al., 2012; Schilling et al., 2013; Kaiser et al., 2013). These studies further reveal that

53 thermal convection in a faulted system generate complex flow patterns either i) within the faults (finger-
 54 like patterns) or ii) across the neighboring permeable aquifers (convective roll or helicoidal patterns).
 55 An example in which these modes of convection might coexist is the Lower Yarmouk Gorge (LYG), at the
 56 border between Israel, Jordan and Syria (Fig. 1). In the LYG, thermal waters ascend through fractured
 57 aquicludes forming hot springs. The latter occur over wide areas forming clusters that are close to or
 58 along the major fault axis. Groundwater temperatures within the same cluster of springs (Fig. 1) strongly
 59 vary. Particularly, in the LYG clusters, the temperature difference between springs or artesian wells that
 60 are less than 50 m apart can be more than 10 °C.

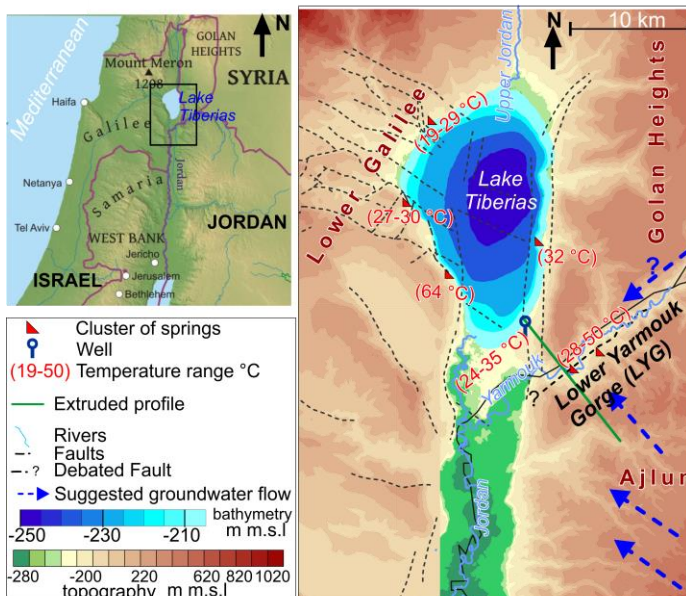


Figure 1. Clusters of thermal springs (red triangles) occur all around Lake Tiberias and within Lower Yarmouk Gorge (LYG). Multi-directional groundwater flow from heights and buoyancy forces through faults generate the Lower Yarmouk Gorge (LYG) cluster of springs. Each cluster represents wide areas where different thermal springs are observable.

61
 62 Hydrochemical studies from Siebert et al. (2014) indicate an intense anisotropic hydraulic functionality
 63 of the lower gorge that allows for both channeled groundwater flow along the longitudinal axle (E-W)
 64 and cross-cutting nearly meridional flow.

65 Previous 2D models from Magri et al. (2015) suggested that the LYG hot springs (Fig. 1) are a mixture of
 66 groundwater from the surrounding highlands (topography-driven flow) and thermal fluids ascending
 67 along faults (buoyancy-driven flow). However, the two-dimensional limitations of the simulations did
 68 not allow to fully capture convective patterns that cross-cut the major flow direction nor those that may

69 develop within the fault plane. Here an idealized 3D model of thermal convection in a faulted system is
70 built with the aim to study the development of different modes of convection, likely responsible of
71 upsurge of thermal water. Owing to the generalized structural features of the studied domain, the
72 results presented here illustrate both 2D and 3D modes of thermal convection that can characterize any
73 faulted hydrothermal systems and are not strictly related to the LYG. The interactions between different
74 convective modes in 3D unveil new mechanisms supporting the existence of complex transboundary
75 flow paths across faults, to date only traceable with hydrochemical investigations (e.g. Siebert et al.,
76 2014). This article further applies recently developed formulas to predict the onset of convection of
77 temperature-dependent viscous fluids in 3D faults (Malkosvky and Magri, 2016).
78 First, the numerical implementation applied to both 2D and 3D models is described. Then 2D and 3D
79 flow and heat patterns are compared. The concluding remarks about the inferred flow paths outline
80 general implications for thermal water migration in faulted hydrothermal systems, such as the LYG.

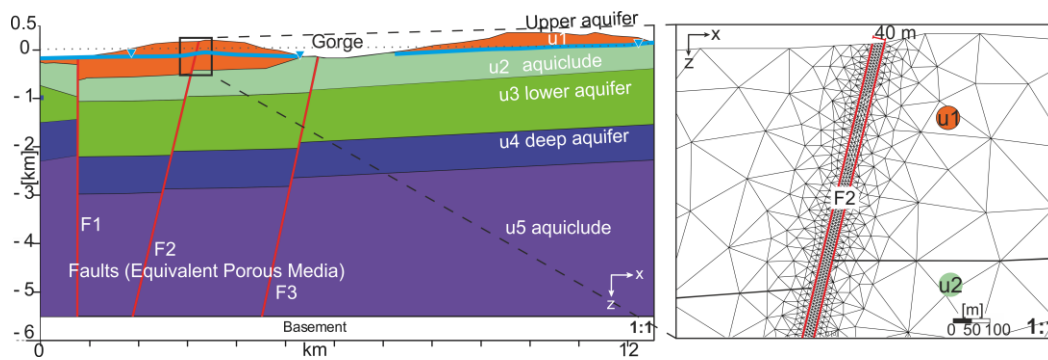
81 **2. Numerical implementation**

82 The equations governing coupled fluid flow and heat transport processes are solved using the finite
83 element software FEFLOW[®]. The mathematical formulation is given in Diersch (2014) and will not be
84 recalled here. A semi-implicit time discretization scheme with a maximum time step of 3 years advances
85 the coupled equations over 1 million year (Myr) for both 2D and 3D models. The simulated time interval
86 of 1 Myr does not represent a specific geological period but allows the simulations to reach a quasi
87 steady-state solution.

88 **2.1 2D / 3D domains and faults**

89 For the scope of this study, the LYG and its major hydrogeological features served as base for building
90 2D and 3D numerical models. The geometry of the two-dimensional domain illustrated in Figure 1 is
91 adapted from the conceptual model given in Magri et al. (2015). The profile extends over 12 km and a
92 500 m thick closing unit, labeled “basement”, closes the model at 6.4 km depth (Fig. 2a). This additional

93 layer serves as thermal buffer between bottom heat boundary conditions and the overlying 2.5 km unit
 94 of Triassic carbonate and marly rocks (u5), which structure is to date poorly constrained. The cross-
 95 section includes a 0.5 km thick Jurassic unit made of partly karstified limestones and shales (u4). Above,
 96 Cretaceous rocks form the lower aquifer (u3), primarily composed of sand-, lime- and dolostone with
 97 interbedded marls. Early Tertiary marls and chalk compose the u2 aquiclude, which form the LYG floor
 98 and the base of its shoulders. The latter are topped by a ca. 200 m thick Tertiary limestone aquifer (u1),
 99 which is partly covered by conductive basalts. The gorge's shoulders quickly reach elevations of 200 m to
 100 400 m mean sea level (MSL) and continue into heights of 800-1000 m MSL elevation. The 2D models by
 101 Roded et al. (2013) and Magri et al. (2015) show that the measured log temperatures and the increased
 102 geothermal gradient of the LYG are better fitted with the presence of faults or areas with enhanced
 103 vertical permeability. Here three normal faults represented as equivalent porous media (EPM) of 40 m
 104 width cut the aquifer system in its entire thickness.

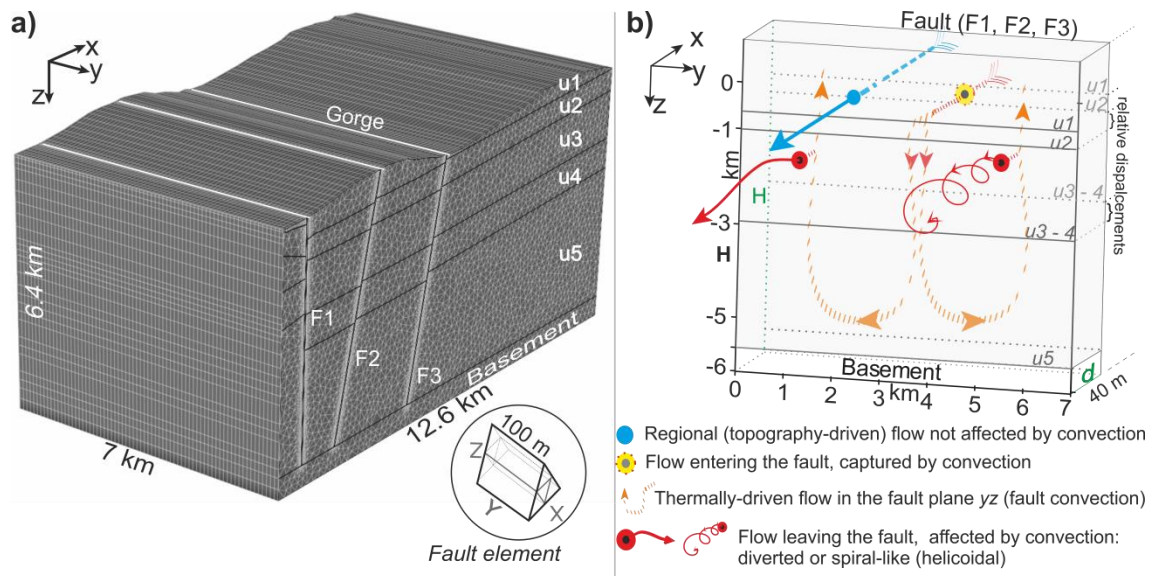


105 **Figure 2.** Stratigraphy of the studied profile, including head level (blue line) used as flow boundary condition. The profile is
 106 adapted from the LYG example described in Magri et al. (2015) and constitutes a schematic approach. A zoom of the finite
 107 element mesh in the xz plane shows the grid refinement in the faults. The latter are modeled as 40 m wide Equivalent Porous
 108 Media (EPM).
 109

110 The “Triangle” algorithm (Shewchuk, 1996) is used to discretize the xz domain in finite elements with
 111 variable width (Fig. 2, zoom). Within the faults, the mesh resolution is approximately 10 meters, i.e. at
 112 least four nodes discretize the fault aperture in the x-direction. Element spacing grows gradually from
 113 the fault flanks to 50 meters in the surrounding units and basement.

114 The 3D solution domain is obtained by extruding the 2D mesh over 7 km in the y -direction (Fig. 3a). In
 115 total, the 3D model comprises 2.4 million prismatic elements with a constant resolution of 100 m in the
 116 y -direction (Fig. 3a). Accordingly, the faults are 40 m thick, 7 km long and approximately 5.5 km deep
 117 EPM block units. The 3D faults account for the relative displacement of the surrounding aquifers
 118 (Fig. 3b). The resulting 3D structural model is not reproducing the real structural characteristics of the
 119 LYG and is solely used as a conceptual model to investigate the evolution of convective modes in 3D.

120 The implementation of faults as EPM is preferred to planar or 2D discrete elements because it allows to:
 121 i) study topography- and thermally- driven flow interactions within cutting permeable units (e.g.
 122 helicoidal flow, Fig. 3b); ii) implicitly solve conductive lateral heat exchange between fault walls and
 123 adjacent aquifers that trigger thermal convection iii) apply the theory from Wang et al. (1987),
 124 Malkovsky and Pek (2004) to determine the onset of thermal convection within the faults. This latter
 125 process is henceforth referred to as fault-convection in the fault plane yz (Fig. 3b).



126
 127 **Figure 3. a)** The 3D mesh is made of 2 341 850 triangular prisms of 100 m length (y -direction) and variable resolution in the xz
 128 plane (see figure 1, xz cross-section and zoom). **b)** Schematic representation of the modeled 3D faults. Faults are 40 m thick, 7
 129 km long and ~ 5.5 km deep EPM units. The yz surface cutting the fault is referred to as fault plane. Three different types of flow
 130 patterns involving the fault are illustrated: i) advective flow that is not affected by thermal-convection (blue line), as by example
 131 shallow or confined regional flow flowing through the fault; ii) fault-convection, i.e. convective flow developing in the fault
 132 plane, parallel to the yz plane (orange dashed lines) and iii) spiral-like flow indicating the interaction between convective and
 133 advective flows. In both figures, the unit numbering (u1 to u5) refers to the stratigraphy given in Figure 1 and Table 1.

134 2.2 Physical properties of rocks and fluids

135 The physical properties of each unit (e.g. hydraulic conductivity, porosity and heat conductivity) are
 136 given in Table 1. The assigned values are large-scale averages derived from previous hydrogeological
 137 investigations, field studies and lithological descriptions as detailed in Magri et al. (2015). The 2D and 3D
 138 models differentiate the main aquifers and aquitards in the vertical direction (z). The anisotropy ratio of
 139 host rocks (K_z/K_x) is 0.015 while faults are isotropic. For each simulation, three faults are given identical
 140 hydraulic conductivity, which values vary between $2.3e^{-7}$ m/s and $9.3e^{-7}$ m/s (i.e. 7 m/yr and 30 m/yr,
 141 respectively). The faults and the upper aquifer have hydraulic conductivity values of the same order of
 142 magnitude, whereas the Lower aquifer (u3) can be up to 10 times more permeable than cutting units. In
 143 other words, faults do neither enhance nor prevent groundwater flow in the direction perpendicular to
 144 the fault plane.

145

Units Label	Type of unit	Hydraulic conductivity K (m/s)	Thermal conductivity λ^s (W/m/°C)	Porosity ϕ
u1	Upper aquifer	$2.7e^{-07}$	2.10	0.06
u2	Aquitard	$3.2e^{-08}$	1.50	0.08
u3	Lower aquifer	$2.1e^{-06}$	2.24	0.13
u4	Lower aquifer	$7e^{-07}$	2.50	0.04
u5	Aquiclude	$3e^{-10}$	2.70	0.01
(F)	EPM	$9.3e^{-07}$; $4.6e^{-07}$; $2.3e^{-07}$	1.1	0.2
Basement		$1.2e^{-12}$	2.50	0.01

152

153 **Table 1.** Physical properties of the modeled units. Values are large-scale averages derived from different hydrogeological
 154 studies as listed in Magri et al. (2015). Read $1.2e^{-12}$ as 1.2×10^{-12} . Longitudinal and transversal dispersivity are null, i.e. the
 155 tensor of thermodispersion is $\Lambda = \phi\lambda^f + (1-\phi)\lambda^s$.

156 Fluids properties are summarized in Table 2. The polynomial fittings of Magri et al. (2015) are used to
 157 compute variable fluid viscosity μ^f and density ρ^f over the pressure and temperature ranges of the

158 solution domain. No concentration effects are accounted because of the low salinity that characterize
 159 the western LYG groundwater. Fluid thermal conductivity λ^f and heat capacity c^f are constants at
 160 reference temperature of 20 °C.

161

162

Fluid property	Value
Thermal conductivity λ^f (W/m/°C)	0.65
Volumetric heat capacity $\rho^f c^f$ (J/m ³ /°C)	4.2e ⁶
Fluid density ρ^f (kg/m ³)	Variable
Fluid viscosity μ^f (Pa/s)	Variable
Coefficient of thermal expansion β (°C ⁻¹)	Variable

163

164

165

166

167

168

169

170 **Table 2** Fluid properties. Variable fluid properties are pressure and temperature dependent expressions computed with the
 171 polynomial fittings given in Magri et al. (2009). Read 4.2e6 as 4×10^6 (computed with an Equation of State). For the Rayleigh
 172 calculations the used values are those at reference temperature and pressure (i.e. minima values). No salinity effects are
 173 accounted in the simulations.

174 2.3 Boundary and initial conditions

175 2D and 3D models use identical boundary conditions, as follows: The groundwater levels vary
 176 from -200 m MSL at the left ending of the domain to 50 m MSL at the right ending. Though these
 177 piezometric measurements are characteristics of the LYG, they induce a steady state regional flow over
 178 the 12 km domain extension that can be encountered in any basin system, where highlands and
 179 lowlands act respectively as recharge and discharge areas. When a hydraulic gradient is imposed to a
 180 thermal buoyant flow, the resulting process is called mixed convection. By contrast, in a free thermal
 181 regime, no regional flow exists. For the specific case of free thermal convection, a flat head boundary
 182 condition is set at the top of the domain. No flux boundary conditions are assigned on the lateral sides
 183 and bottom of the domain. The temperature at the top of the domain is allowed to vary with respect to
 184 convective heat transfer through a Cauchy boundary condition. The reference temperature is 20 °C. A

185 constant heat flow of 60 mW/m² is imposed at the basement. Lateral boundaries are thermally
186 insulated.

187 The initial conditions for head and temperature distributions are derived from steady state simulations
188 of groundwater flow and conductive heat transport, respectively.

189 3. Results and discussions

190 3.1 2D results

191 Linear stability analysis based on Rayleigh number calculations offers a useful tool to determine the
192 onset of thermal convection (e.g. Nield, 2006). The Rayleigh number is:

$$193 R = \frac{Kd\beta\Delta T}{D_\lambda} \quad (1)$$

194 where K (m/s) is the hydraulic conductivity of the aquifer, β (1/°C) is the coefficient of thermal
195 expansion and ρ^f (kg/m³) the fluid density. ΔT (°C) is the variation of temperature over the aquifer

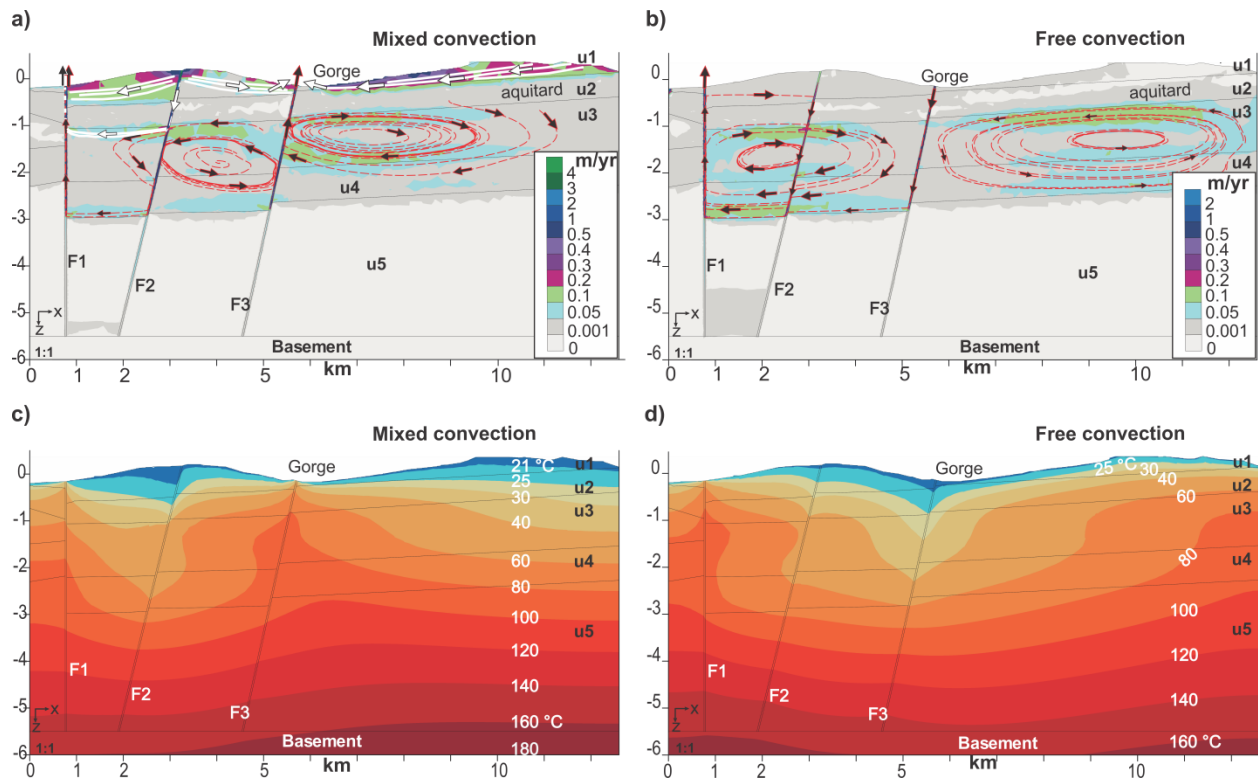
196 thickness d (m). $D_\lambda = \frac{\phi\lambda^f + (1-\phi)\lambda^s}{\rho^f c^f}$ (m²/s) is the tensor of thermodispersion where c^f (J/kg/°C) is

197 the specific heat capacity of the fluid, λ^f and λ^s (W/m/°C) are the thermal conductivity of fluid and
198 solid, respectively.

199 Considering units u3 and u4 define together a 2 km aquifer (Fig. 2, Fig. 3) with thickness-weighted
200 average values for porosity, permeability and heat conductivity of 0.1, 1.4e⁻⁶ m/s and 2.4 W/m/°C and
201 assuming that $\Delta T \approx 60$ °C over the 2 km thick aquifer and estimating that therein $\beta \approx 3e^{-4}$ °C⁻¹, then:

$$202 R \approx \frac{1.4e^{-6} \times 2000 \times 3e^{-4} \times 60}{(0.1 \times 0.65 + (1-0.1) \times 2.4) / 4.2e^6} = 95$$

203 which is higher than $4\pi^2$, the critical Rayleigh number R_c for an infinitely long homogenous porous
 204 media (Lapwood, 1948). This analytical estimation suggests that thermal convection likely develops
 205 within the lower aquifers, as shown by the numerical simulations. 2D results of coupled fluid flow and
 206 heat transport processes are illustrated for both mixed and free convection in Figure 4 for the case
 207 $K_{fault} = 9.3e^{-7}$ (m/s), i.e. 30 m/yr.



208 **Figure 4.** 2D results. **a-b)** Darcy velocity (m/yr), and **c-d)** temperature (°C). Mixed convection regime (**a-c**) occurs when
 209 topography- and thermally-driven flow interacts (white and red pathlines, respectively). Free convection (**b-d**) refers to a purely
 210 buoyant-driven flow simulated with a flat head boundary condition at the top, preventing any imposed regional flow.
 211

212 In both cases, two convective cells develop in the lower aquifers u3 and u4 at each side of the fault F3
 213 (Fig. 4a; b). The cells are layered and bounded at the top and bottom by the aquitards u2 and u5,
 214 respectively. Convection circulates deep groundwater at peak velocity of 0.2 m/yr. The flow boundary
 215 condition at the top controls the direction of convective circulation: In the mixed convection regime (Fig.
 216 4a), the cells drive thermal water upward in the “gorge fault” F3, whereas in the free regime (Fig. 4b) the
 217 flow along the F3 fault is downward. As a consequence, the number of protruding thermal plumes

218 differs in each scenario (Figs. 4c; d). The mixed convective regime generates two thermal plumes
219 reaching the surface (Fig. 4c). In this case, the simulated spring temperatures range between 40 °C and
220 50° C. In the free thermal regime (Fig. 4d), the temperature gradient below the gorge is decreased. Only
221 the discharging fault F1 at the left ending of the profile flushes thermal water at temperature close to
222 60 °C. In both mixed and free convective regimes, no thermal convection develops within the faults.
223 These EPM units act as preferential pathways for either ascending or descending groundwater. In 2D
224 only one flow direction is possible within the fault.

225 The described patterns are sufficient to highlight the general mechanisms of coupled fluid transport
226 processes, namely topography-driven flow (regional flow) superimposed to thermal convection that
227 occurs in many faulted hydrothermal systems. The resulting mixed convective regime can explain flow
228 directions along faults and related increased/decreased temperature gradients. However, because of
229 their 2D constraints, the models cannot capture modes of convection that are parallel to the fault plane
230 (i.e. perpendicular to the described profile) thereby impeding any comparison between the spatial
231 distribution of convective cells and the occurrences of thermal springs along the fault trace. The next 3D
232 simulations are aimed to study the interaction between fault convection (Fig. 3b, orange cells) and
233 crosscutting groundwater flow, which can be either regional flow (Fig. 3b blue vector) or thermal
234 convective flow in the surrounding aquifers (Fig 3b, red vectors).

235 **3.2 3D Results**

236 Wang et al. (1987) demonstrated that the critical Rayleigh number R_c of 3D vertical faults embedded in
237 impervious rocks is inversely proportional to the fault aspect ratio (fault width/height), i.e. referring to
238 Figure 2b, $R_c \propto O(H / d)$. Malkovsky and Pek (2004) provided an analytical relationship to calculate R_c
239 values, for the case of a fault with a permeable top, as follows:

240
$$R_c = \left[\left(\frac{6.428}{\Delta} \right)^{1.165} + (27.1)^{1.165} \right]^{0.8584}, \text{ with } \Delta = \frac{d}{2H} < 0.1 \text{ (half of the aspect ratio)} \quad (2)$$

241 Tournier et al. (2000) calculated similar values of critical Rayleigh numbers by means of numerical
 242 simulations. Furthermore, their numerical benchmarks showed that at those R_c , thermal convection in
 243 the fault is triggered after a certain time-period and therefore is also referred to as delayed convection.
 244 A limitation of the mentioned studies is that fluid viscosity is constant, although small viscosity changes
 245 can exert a substantial influence on conditions for onset of free thermal convection (Zhao et al., 2006).
 246 Recent analytical and numerical investigations by Malkovsky and Magri (2016) estimated that in a
 247 faulted geothermal system under normal temperature conditions as those modeled here, variable fluid
 248 viscosity triggers thermal convection within faults which permeability is four times lower than in the
 249 case of a fluid with constant viscosity. In this study, since fluid viscosity is temperature dependent, it is
 250 assumed that fault convection occurs at $R_c / 4$ where R_c is estimated at lowest temperature conditions
 251 In the studied case (Fig. 3b), $\Delta \approx 40 / (2 \times 5500) = 3.6e^{-3}$ (half aspect ratio) leading to the critical
 252 Rayleigh number (Eq. 2) $R_c \approx 1780 / 4 = 445$ for a temperature-dependent viscous fluid.

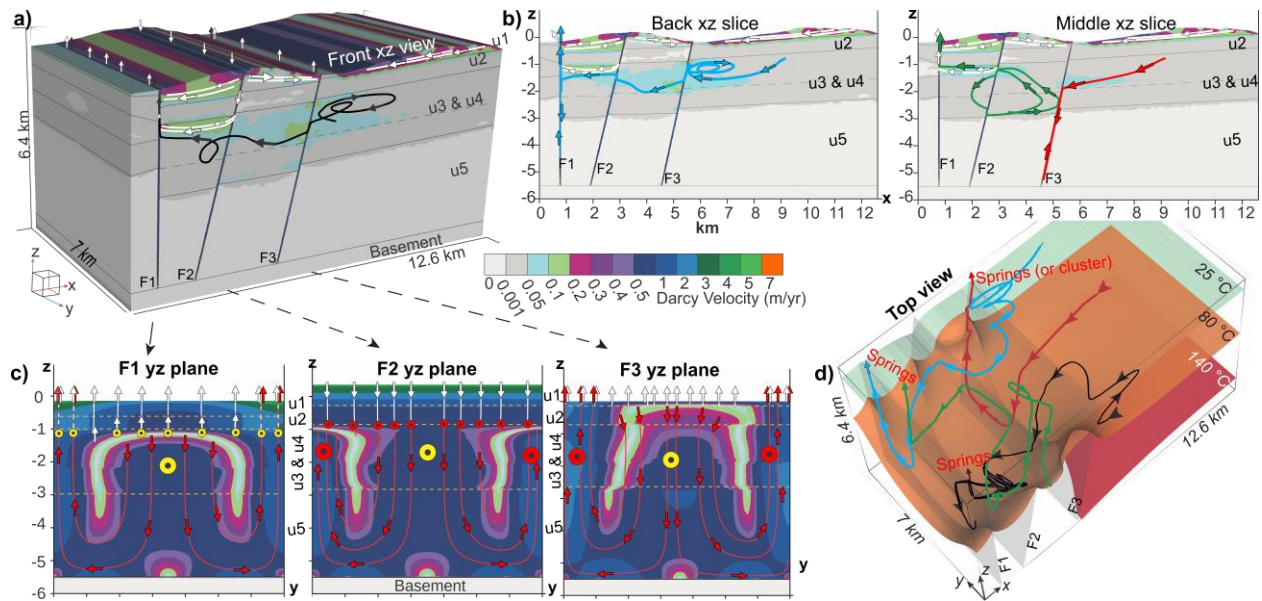
253 The critical hydraulic conductivity value of the fault, K_{crit} , that corresponds to $R_c = 445$ can be derived
 254 from Eq. 1, using the fault and fluid properties given in Table 1 and Table 2, respectively. Estimating that
 255 over the 5500m deep fault $\Delta T \approx 140$ °C, a thermal expansion coefficient $\beta \approx 5.9.e^{-4}$ °C⁻¹ provides a
 256 good fluid density fit (e.g. Fig. 4 in Malkovsky and Magri, 2016) then:

257
$$K_{crit} \approx \frac{445 \times (0.2 \times 0.65 + (1 - 0.2) \times 1.1) / 4.2e^6}{5500 \times 5.9e^{-4} \times 140} \approx 2.4e^{-4} \text{ m/s}$$

258 i.e. fault convection is favored at $K_{fault} = 9.3e^{-7}$ m/s and $K_{fault} = 4.6e^{-7}$ m/s (Table 1). At $K_{fault} < 2.4e^{-7}$
 259 the thermal regime is purely conductive.

260 In narrow apertures, the fault plane yz is the preferred mode of convection (Simmons et al., 2008), and
261 consists of weakly three-dimensional square cells (Wang et al., 1987), as illustrated by orange cells in
262 Figure 2b. The next 3D simulations will provide insights into the interactions between fault convection
263 and lateral cross-cutting regional flow.

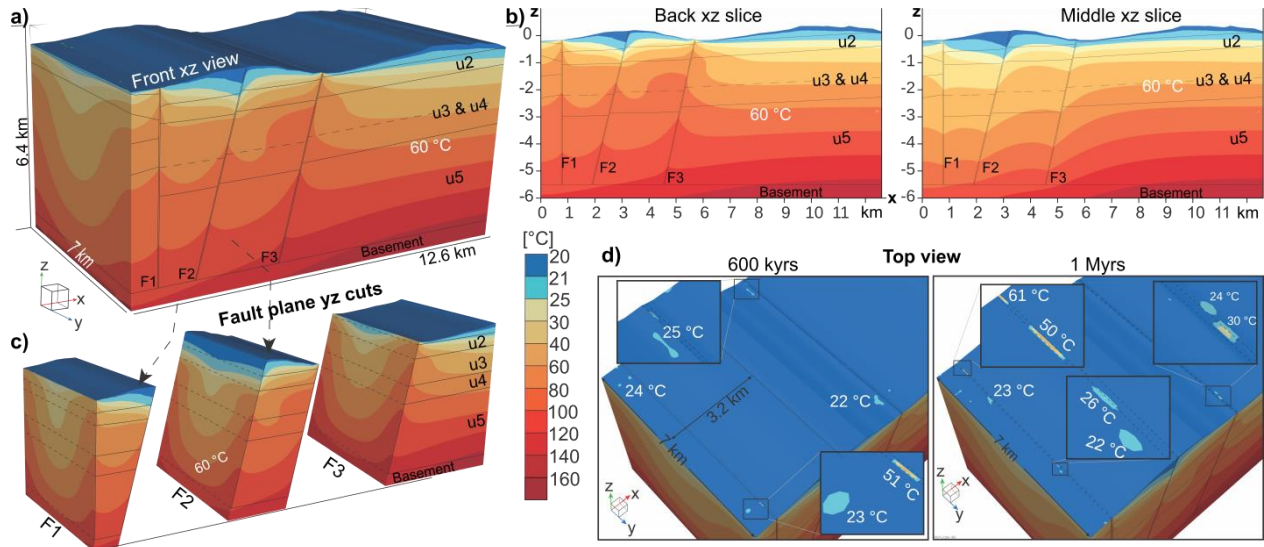
264 Results of 3D mixed convective flow are illustrated in Figure 5 for the case $K_{fault} = 9.3e^{-7}$ m/s (i.e.
265 30 m/yr). The cross-sectional views parallel to the regional flow (Figs. 5a; b) reveal that fluid convection
266 can develop within the major aquifers $u3$ and $u4$. The location and shape of the cells however differ
267 from the 2D case (compare with Figure 4a). By example, in the middle slice (Fig. 5b), groundwater flows
268 from the right ending of the profile directly toward the F3 fault, whereas in 2D the aquifers are
269 characterized by a persistent convective regime adjacent to the faults and a bounded regional flow in
270 the top $u1$ aquifer (Fig. 4a). In 3D, multi-cellular motion is dominant in each fault plane (Fig 5c), as
271 predicted by analytical calculations. Within the faults, two elongated convective cells stretch over the
272 entire fault height. The cellular motion consists of a central downflow and two lateral upflows at
273 velocities ranging between 0.5 m/yr and 2 m/yr, respectively. Therefore, inflow and outflow of
274 groundwater can occur within the same fault over its entire length (i.e. y -direction). Fault convection
275 allows groundwater to reach basement depths where it gets heated before starting its upward
276 migration within the fault. During this process, two scenarios are then possible: i) thermal water
277 discharges through the fault surface mixing with the regional flow (red and white arrows in Fig. 5c) ii)
278 ascending thermal water interacts with the advective regional flow that enters the fault through the
279 intersecting $u3$ and $u4$ aquifers (yellow circles in Figure 5c). In the latter case, the direction of the
280 regional flow outside the fault is deviated or undergoes complex helicoidal (spiral-like) patterns (red
281 circles in Fig. 5c), as illustrated in the 3D rendering (Fig. 5d).



282
 283 **Figure 5.** Mixed convection. $K_{fault} = 9.3e^{-7}$ m/s (i.e. 30 m/yr). Flow paths plotted over the velocity field (meter per year) for
 284 different views. Cross-sectional xz views (a - b) show and the upper regional flow (white lines and vectors) as well as different
 285 cross-sectional convective patterns (black, blue, green and red lines) in the aquifers u3 and u4. Fault plane yz views (c) indicate
 286 that two convective cells develop in each fault (red lines, vectors). Groundwater entering/leaving the fault perpendicular to the
 287 fault plane (i.e. in the x direction) is schematically represented with a red/yellow circle, as also explained in figure 2b. White
 288 arrows depict regional flow recharge/discharge areas (d) The black, blue, green and red flow paths as shown in a)-b) are also
 289 plotted in a 3D top view revealing complex heliocidal flow patterns. As a result, thermal water can discharge at different
 290 locations forming cluster of springs close to fault traces.

291 The coexistence of these flow processes, namely regional flow in the aquifers and convection within the
 292 fault, strongly impacts the temperature field (Figs. 6a; b). Temperature decreases in the center of the
 293 fault, in relation to downward flow and increases along the fault sides (Fig. 6c). Furthermore the spacing
 294 between thermal plumes is controlled by cellular motion in the faults. Accordingly, the temperature
 295 profiles vary also along the y-direction (i.e. xz cross-sections perpendicular to the fault plane, Fig. 5b), in
 296 contrast to the purely two-dimensional case (Fig. 4c). As the regional flow determines the location of
 297 the discharge areas, springs form at the top of F1 and F3 faults. Along those fault traces, the locations of
 298 springs correspond to the wavelength of the underlying convective cell. However, since the convection
 299 is highly transient in nature, a given spring might shift along the fault trace, depending on the periodicity
 300 of the cellular motion (Fig. 6d). Springs temperature can reach 60°C. An additional simulation in which
 301 $K_{fault} = 4.6e^{-7}$ m/s (i.e. 14.5 m/yr) computed qualitatively very similar flow patterns. The only observed

302 differences are lower convective velocities and less decreased temperature field in the central part of
 303 the faults.



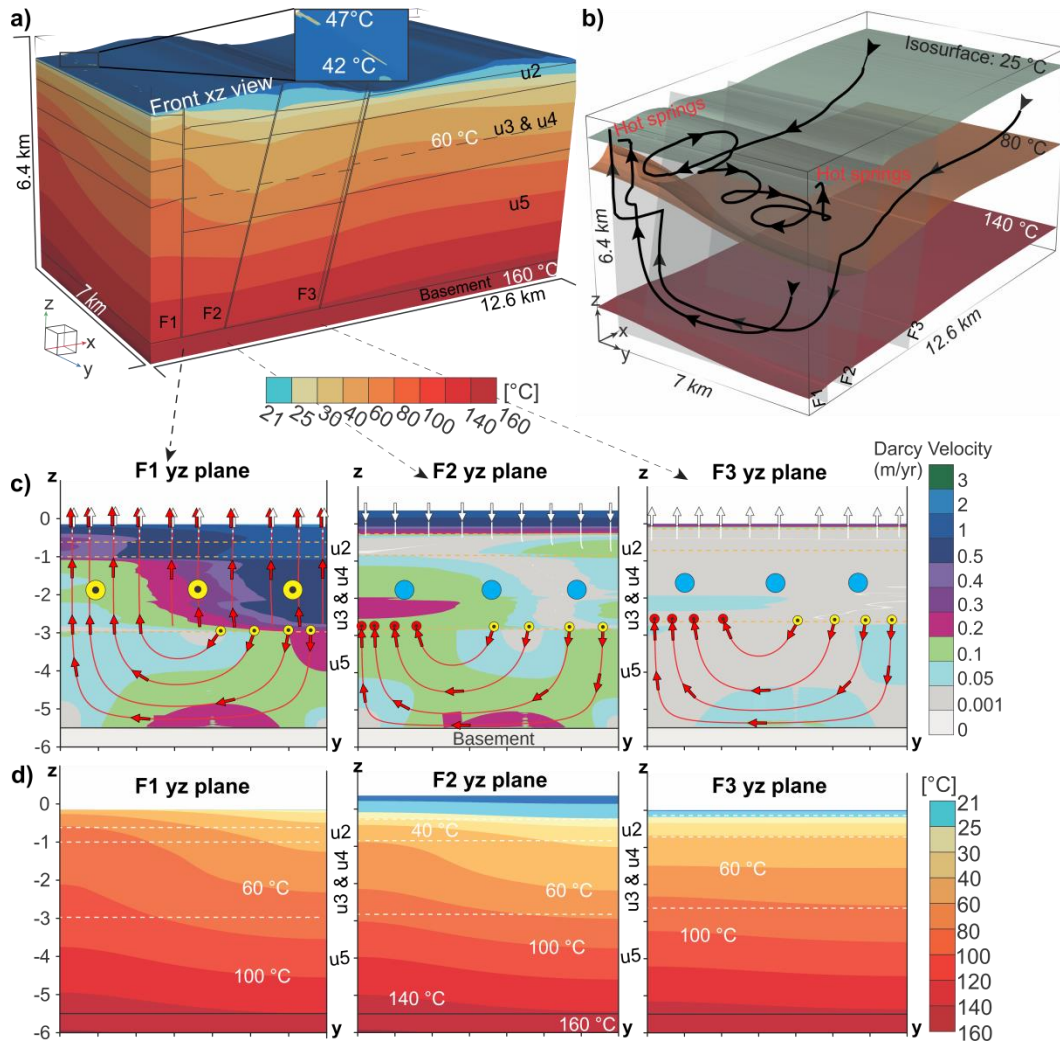
304
 305 **Figure 6.** Mixed convection. $K_{fault} = 9.3e^{-7}$ m/s (i.e. 30 m/yr). Calculated temperature ($^{\circ}$ C). Thermal plumes are illustrated along
 306 different cross-sectional xz views (a - b). Fault plane yz views (c) show the effects of convection: temperature decreases in the
 307 central part of the fault and increase at both lateral sides. The 3D top views (d) at 600,000 years and 1,000,000 years indicate
 308 that thermal springs can shift over time along fault traces because of the transient nature of fault convection. Zooms of the
 309 clusters (black rectangles in (d)) show that the temperature difference between closely interspaced springs can be more than
 310 10° C. Simulations with $K_{fault} = 4.6e^{-7}$ m/s (i.e. 14.5 m/yr) display very similar general features.

311 In the next simulation, the hydraulic conductivity of the fault is $K_{fault} = 2.3e^{-7}$ m/s (i.e. 7.2 m/yr). Here it
 312 is worth recalling that the faults are 3 to 10 times less permeable than the aquifers u4 and u3,
 313 respectively (Table 1). However, the relatively small thickness of the faults with respect to the km-scale
 314 extension of the study domain does not prevent advection across the faults. A striking result is the onset
 315 of fault convection despite the simulated hydraulic conductivity of this scenario falls below the
 316 previously estimated critical value of $2.4e^{-7}$ m/s. Compared to the previous cases ($K_{fault} = 9.3e^{-7}$ m/s and
 317 $K_{fault} = 4.6e^{-7}$ m/s), the thermal plumes in the F2 and F3 faults are smoothed (Fig. 7a) suggesting that
 318 therein the regional flow does overwhelm thermally-driven flow. However, the convective and helicoidal
 319 3D flow paths (Fig. 7b) close to the F1 fault indicate that buoyant and thermal forces still interact within
 320 discharge areas. The fault plane views of the velocity field (Fig. 7c) further clarifies the ongoing

321 processes: groundwater flows into the upper 3 km of the faults through the permeable aquifers u3 and
322 u4 (Fig. 7c, blue circles) at velocities between 0.1 m/yr and 3 m/yr whereas, at Triassic depths, a single
323 elongated convective cell drives thermal water in the fault plane at maximum velocity of 0.2 m/yr. The
324 thermal water exits the F3 and F2 faults along the top Triassic (Fig. 7c, red circles) to eventually
325 discharge at the surface of the F1 fault where temperatures can locally be higher than 40 °C (Figs. 7a; d).
326 Without the regional flow (free convection), the simulated thermal regime remains purely conductive, in
327 agreement with the analytical calculations previously described. Therefore, the presence of deep-seated
328 convective cells within less permeable faults is due to the crosscutting regional flow that transports
329 additional lateral heat to the fault walls, thereby triggering buoyancy.

330

331

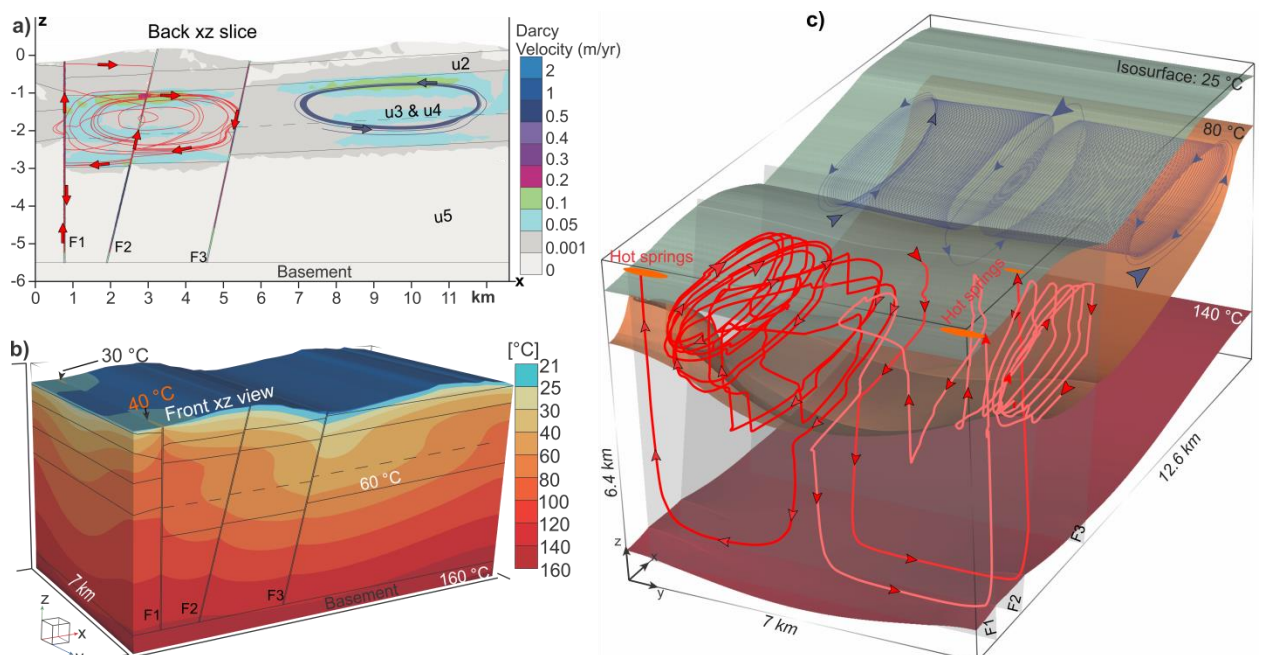


332
 333 **Figure 7.** Mixed convection. $K_{fault} = 2.3e^{-7}$ m/s (7.25 m/yr). (a) 3D front view of the calculated temperature (°C). Within a
 334 predicted cluster of springs, temperature varies of 5°C (b) 3D flow paths show both fault convection and helicoidal features. (c)
 335 Fault plane yz views of the velocity field (m/yr) indicate that one convective cells develop in each fault, at Triassic depth (red
 336 lines, vectors). By contrast, the regional flow is dominant in the upper fault entering F2 and F3 through intersecting aquifers
 337 (blue circles). Thermal water enters/leaves the fault along the top permeable aquifer u4. (yellow/red circles). Groundwater
 338 captured by fault convection in F1 (yellow circles) discharges at the surface mixing with regional flow (white arrows). The
 339 resulting temperature field (d) is illustrated at each fault plane yz views.

340 In their pioneering simulations of hydrothermal circulation in fault zones, Lopez and Smith (1995)
 341 mapped permeability ranges that delimit the transition from convective to advective regimes. They
 342 found that in a permeable fault zone, convection is favored over advection when the permeability of the
 343 country rock is lower than given values, in agreement with the numerical observations presented here.
 344 In this specific scenario, the estimated hydraulic conductivity of the hosting rock that favors convection
 345 in the fault is $K \leq 7e^{-7}$ m/s (Table 1). While Lopez and Smith (1995) consider a fault cutting a single

346 aquifer, here it is suggested that in a system characterized by multilayered aquifers, different transport
 347 regimes can coexist within a fault zone as the result of the interplay between pressure forces and
 348 buoyancy. In this respect, permeability distributions of the surrounding aquifers and fluid density
 349 variations play a key role as they respectively control advective fluxes and buoyant forces.

350 A final simulation of free convective flow is carried out for the case $K_{fault} = 4.6e^{-7}$ m/s (14.5 m/yr), i.e. at
 351 conditions favoring fault convection. Results are illustrated in Figure 8. It can be seen that patterns and
 352 values of both velocity and temperature fields (Fig. 8a; b) are very close to the two-dimensional results
 353 shown in Figures 4b and 4d. In 3D, the anti-clockwise convective cell at the right side of the F3 fault
 354 extends over the y-direction forming elongated rolls. At the intersection with fault cells, these rolls
 355 assume spiral-like shapes, as it can be seen in Figure 8c, close to the F1 and F2 faults. The mechanism is
 356 analogous to the previously explained mixed convective case, where the interactions between thermal
 357 convection in the fault plane and the imposed transversal regional flow led to helicoidal flow patterns.



358 **Figure 8.** Free convection. $K_{fault} = 4.6e^{-7}$ m/s (i.e. 14.5 m/yr). **(a)** Flow paths plotted over the velocity field (m/yr) for a cross-
 359 sectional xz view **(a)** 3D front view of the calculated temperature (°C). **(b)** 3D flow paths show convective rolls (blue cells) and
 360 fault convection. The interaction between these two processes generates spiral-shaped flow patterns **(c)**.
 361
 362

363 **Conclusions**

364 Though based on simplified structural hydrogeological features, the simulations presented here
365 provided insights into the possible interactions between deep flow processes in faulted basins that could
366 not be inferred from 2D studies. Specifically, the sensitivity analysis of the fault permeability showed
367 that faults crosscutting the main regional flow direction allow groundwater to be driven laterally by
368 convective forces within the fault planes (Figs. 5 and 7). Therein thermal waters can either discharge
369 along the fault traces or exit the fault through adjacent permeable aquifers. In the latter case, the
370 resulting flow is helicoidal and transient (Figs. 5d; 7c; 7d). Accordingly, the location of discharge areas
371 can move with time and is not strictly constrained to the damage zones (Fig. 6d). The spacing between
372 cluster of springs reflects the wavelength of the multicellular regime in the fault zone. Vigorous regional
373 flow favors deep layered convection within fault planes by enhancing lateral heat transfer to the fault
374 walls. Simulations show that both regimes can coexist also at values of fault hydraulic conductivity
375 below critical Rayleigh conditions (Fig. 7). By contrast, when the regional flow is weak or totally absent,
376 as in free convection (Fig. 8), fault convection is triggered only above Rayleigh conditions, as predicted
377 by the viscous-dependent analytical solutions from Malkovsky and Magri (2016). Furthermore, in a free
378 convective regime, convective rolls similar to those observed in the 2D case (Figs. 4b; d) extend
379 throughout the entire aquifer length (Fig. 8c). The interactions between these 2D-like convective rolls
380 and planar fault cells generate spiral-like transient patterns, as those observed in the mixed convective
381 regime.

382 The idealized numerical models presented here suggested possible transport mechanisms that can, for
383 example, be applied to the LYG (Fig. 1) where thermal water ascends through fractured aquicludes and
384 the hydrochemical character of the emerging groundwaters is disparate. Investigations on rare earth
385 elements, major elements and stable isotopes show that along the level course of the LYG and below
386 the Golan Heights, NE-SW and N-S oriented deep flow paths must exist to permit the chemical

387 composition of the groundwaters in and along the LYG, respectively (Siebert et al., 2014). The idealized
388 numerical models presented here support the hypothesis of crossing flow paths, resulting from the
389 coexistence of fault convection, that can develop for example along longitudinal East-West faults within
390 the Gorge, and additional flow fields that can be induced by topography gradients, e.g. along N-S axe of
391 the Gorge, or by local thermal convection in permeable aquifers below Eocene aquiclude. Given the
392 current estimation of damage zones width (40 m), fault height (5.5 km), and basal heat flow of 60
393 mW/m^2 , a fault hydraulic conductivity of 2.4×10^{-7} m/s (7.2 m/yr) would be sufficient to induce thermal
394 flow in fractured Triassic sediments. Theoretically, deep fluids can migrate through the entire fault
395 length before being flushed in discharge areas by topography-driven flow. At hydraulic conductivity
396 higher than 4.3×10^{-7} m/s (13.6 m/yr), fault convection appears to be controlling heat fluxes also at
397 shallower depths. This highly transient process likely underlies the formation of clustered thermal
398 springs along the Lakeshore. As it is recognized that thermal convection can be a driving mechanism for
399 migration of hydrocarbons (Rabinowicz et al., 1985), the complex helicoidal patterns described here
400 could support the highly debated hypothesis of oil accumulation under sealing caprocks.

401 At the current state, further investigations are being carried out to better constrain the structural
402 features of the basin, such as orientation, depth of penetration and intersections of the faults. For
403 example, numerical calculations from Person et al. (2012) suggest that at given permeability conditions
404 fault intersections focus outflow of hot groundwater. Further aspects that need to be addressed are the
405 effects of aquifer and fault heterogeneities (e.g. Ingebristen and Gleeson, 2014; Lopez and Smith, 1996)
406 and mineral precipitations that can potentially clog faults over the geological time-scale considered
407 here, thereby hindering convective flows (e.g. Genthon et al., 1997).

408 Despite these model simplifications and assumptions, it has been shown that increases of surface
409 temperature near faulted areas fall within measured ranges (20°C - 60°C), suggesting that co-existing
410 modes of thermal convection are likely controlling transboundary flow across the LYG:

411 **Acknowledgment**

412 This research is funded by the German Science Foundation DFG (grant MA4450/2) within the special
413 program to support peaceful development in the Middle East. We greatly acknowledge the DFG for their
414 continuous support. We thank Michael Kühn for the discussions during the simulations process and the
415 anonymous reviewers for their substantial improvements in the paper.

416 **References**

417 Bickle, M.J., 2009. Geological carbon storage. *Nature Geosci* 2, 815-818.

418 Diersch, H.-J.G., 2014. FEFLOW: finite element modeling of flow, mass and heat transport in porous and
419 fractured media. Springer Verlag Berlin Heidelberg.

420 Harcouët-Menou, V., Guillou-Frottier, L., Bonneville, A., Adler, P.M., Mourzenko, V., 2009. Hydrothermal
421 convection in and around mineralized fault zones: insights from two- and three-dimensional numerical
422 modeling applied to the Ashanti belt, Ghana. *Geofluids* 9, 116-137.

423 Gasparrini, M., Bechstädt, T., Boni, M., 2006. Massive hydrothermal dolomites in the southwestern
424 Cantabrian Zone (Spain) and their relation to the Late Variscan evolution. *Marine and Petroleum*
425 *Geology* 23, 543-568.

426 Genthon, P., Schott, J., Dandurand, J.-L., 1997. Carbonate diagenesis during thermo-convection:
427 Application to secondary porosity generation in clastic reservoirs. *Chemical Geology* 142, 41-61.

428 Ingebritsen, S.E., Gleeson, T., 2015. Crustal permeability: Introduction to the special issue. *Geofluids* 15,
429 1-10.

430 Kaiser, B.O., Cacace, M., Scheck-Wenderoth, M., 2013. Quaternary channels within the Northeast
431 German Basin and their relevance on double diffusive convective transport processes: Constraints from
432 3-D thermohaline numerical simulations. *Geochemistry, Geophysics, Geosystems* 14, 3156-3175.

433 Kühn, M., Gessner, K., 2009. Testing hypotheses for the Mount Isa Copper mineralisation with numerical
434 simulations. *Surveys in Geophysics* 30, 253-268.

435 Lapwood, E.R., 1948. Convection of a fluid in a porous medium. *Mathematical Proceedings of the*
436 *Cambridge Philosophical Society* 44, 508-521.

437 López, D.L., Smith, L., 1995. Fluid Flow in Fault Zones: Analysis of the Interplay of Convective Circulation
438 and Topographically Driven Groundwater Flow. *Water Resources Research* 31, 1489-1503.

439 López, D.L., Smith, L., 1996. Fluid flow in fault zones: Influence of hydraulic anisotropy and heterogeneity
440 on the fluid flow and heat transfer regime. *Water Resources Research* 32, 3227-3235.

441 Magri, F., Bayer, U., Maiwald, U., Otto, R., Thomsen, C., 2009. Impact of transition zones, variable fluid
442 viscosity and anthropogenic activities on coupled fluid-transport processes in a shallow salt-dome
443 environment. *Geofluids* 9, 182-194.

444 Magri, F., Inbar, N., Siebert, C., Rosenthal, E., Guttman, J., Möller, P., 2015. Transient simulations of
445 large-scale hydrogeological processes causing temperature and salinity anomalies in the Tiberias Basin.
446 *Journal of Hydrology* 520, 342-355.

447 Magri, F., Akar, T., Gemici, U., Pekdeger, A., 2012. Numerical investigations of fault-induced seawater
448 circulation in the Seferihisar-Balçova Geothermal system, western Turkey. *Hydrogeol J* 20, 103-118.

449 Malkovsky, V.I., Magri, F., 2016. Thermal convection of temperature-dependent viscous fluids within
450 three-dimensional faulted geothermal systems: estimation from linear and numerical analyses. *Water*
451 *Resources Research* 52, 2855–2867.

452 Malkovsky, V.I., Pek, A.A., 2004. Onset of Thermal Convection of a
452 Single-Phase Fluid in an Open Vertical Fault. *Izvestiya, Physics of the Solid Earth* 40, 672-679.

453 Nield, D.A., Bejan, A., 2006. *Convection in porous media*,. 3d edn. Springer, New York.

454 Ormond A., Boulègue J., Genthon P., 1995. A thermoconvective interpretation of heat flow data in the
455 area of Ocean Drilling Program Leg 116 in a distal part of the Bengal Fan. *Journal of Geophysical*
456 *Research: Solid Earth* 100, 8083-8095.

457 Person, M., Hofstra, A., Sweetkind, D., Stone, W., Cohen, D., Gable, C.W., Banerjee, A., 2012. Analytical
458 and numerical models of hydrothermal fluid flow at fault intersections. *Geofluids* 12, 312-326.

459 Rabinowicz, M., Dandurand, J.-L., Jakubowski, M., Schott, J., Cassan, J.-P., 1985. Convection in a North
460 Sea oil reservoir: inferences on diagenesis and hydrocarbon migration. *Earth and Planetary Science*
461 *Letters* 74, 387-404.

462 Rabinowicz, M., Sempéré, J.-C., Genthon, P., 1999. Thermal convection in a vertical permeable slot:
463 Implications for hydrothermal circulation along mid-ocean ridges. *Journal of Geophysical Research: Solid*
464 *Earth* 104, 29275-29292.

465 Roded, R., Shalev, E., Katoshevski, D., 2013. Basal heat-flow and hydrothermal regime at the Golan–
466 Ajloun hydrological basins. *Journal of Hydrology* 476, 200-211.

467 Schilling, O., Sheldon, H., Reid, L., Corbel, S., 2013. Hydrothermal models of the Perth metropolitan area,
468 Western Australia: implications for geothermal energy. *Hydrogeol J* 21, 605-621.

469 Shewchuk, J.R., 1996. Triangle: Engineering a 2D Quality Mesh Generator and Delaunay Triangulator. In:
470 Lin, M.C., Manocha, D. (Eds.), *Applied Computational Geometry: Towards Geometric Engineering*.
471 Springer-Verlag, Berlin, pp. 203-222.

472 Siebert, C., Möller, P., Geyer, S., Kraushaar, S., Dulski, P., Guttman, J., Subah, A., Rödiger, T., 2014.
473 Thermal waters in the Lower Yarmouk Gorge and their relation to surrounding aquifers. *Chemie der*
474 *Erde - Geochemistry* 74, 425-441.

475 Simmons, C.T., Sharp, J.M., Nield, D.A., 2008. Modes of free convection in fractured low-permeability
476 media. *Water Resources Research* 44, W03431.

477 Simms, M.A., Garven, G., 2004. Thermal convection in faulted extensional sedimentary basins:
478 theoretical results from finite-element modeling. *Geofluids* 4, 109-130.

479 Tournier, C., Genthon, P., Rabinowicz, M., 2000. The onset of natural convection in vertical fault
480 planes: consequences for the thermal regime in crystalline basements and for heat recovery experiments.
481 *Geophysical Journal International* 140, 500-508.

482 Wang, M., Kassoy, D.R., Weidman, P.D., 1987. Onset of convection in a vertical slab of saturated porous
483 media between two impermeable conducting blocks. *International Journal of Heat and Mass Transfer*
484 30, 1331-1341.

485 Yang, J., 2006. Finite element modeling of transient saline hydrothermal fluids in multifaulted
486 sedimentary basins: implications for ore-forming processes. *Canadian Journal of Earth Sciences* 43,
487 1331-1340.

488 Zhao, C., Hobbs, B.E., Ord, A., 2008. *Convective Heat Transfer within Three-Dimensional Vertical Faults*
489 *Heated from Below, Convective and Advective Heat Transfer in Geological Systems*. Springer Berlin
490 Heidelberg, pp. 145-159.

491 Zhao, C., Hobbs, B.E., Ord, A., Kühn, M., Mühlhaus, H.B., Peng, S. 2006. Numerical simulation of double-
492 diffusion driven convective flow and rock alteration in three-dimensional fluid-saturated geological fault
493 zones. *Computer Methods in Applied Mathematics and Engineering* 195, 2816–2840.